Mon. Not. R. Astron. Soc. **000**, 1–9 (2012) Printed 24 October 2012 (MN LATEX style file v2.2)

Star formation properties in the Antennae galaxies as seen with Herschel-PACHS — observation vs. simulation

S. J. Karl[1,2,3] ⋆, T. Lunttila[4], T. Naab[3], P. H. Johansson[4], U. Klaas[5] and M. Juvela[4]
[1] *Institute of Astronomy, University of Cambridge, Madingley Road, Cambridge CB3 0AH, United Kingdom*
[2] *Kavli Institute for Cosmology, Cambridge*
[3] *Max-Planck-Institut für Astrophysik, Karl-Schwarzschild-Str. 1, D-85741 Garching bei München, Germany*
[4] *Department of Physics, University of Helsinki, Gustaf Hällströmin katu 2a, FI-00014 Helsinki, Finland*
[5] *Max-Planck-Institut für Astronomie, Königstuhl 17, D-69117 Heidelberg, Germany*

24 October 2012

ABSTRACT
We present a suite of hydro-dynamical numerical simulations of the well-known Antennae galaxies. We find that differences in the gas properties due to variations in the star formation feedback modeling have a much more pronounced impact on the resulting FIR properties, than any variations in the assumptions of our (rather simplified) post-processing procedure (give values here!). Our results are relevant for future observations of star formation tracers in the Antennae galaxies in the infrared (e.g. Herschel, ALMA, etc.).

Key words: methods: numerical – galaxies: evolution – galaxies: individual: NGC 4038/4039 – galaxies: interactions – galaxies: star formation.

1 INTRODUCTION

We want to study the merger-induced star formation in the Antennae. Especially interesting, of course, is the peculiar overlap starburst. By direct comparison with detailed multi-wavelength observations we can test and possibly constrain the star formation algorithm used in GADGET 2 & 3. In particular, we aim to put limits on the strength of the applied stellar feedback by choosing three (bracketing) cases of the parameter for the softened equation of state, namely the 'standard' full feedback model with $q_{\rm EOS} = 1.0$, an intermediate model with $q_{\rm EOS} = 0.5$, and a model with very weak feedback $q_{\rm EOS} = 0.01$, i.e. very close to isothermal.

2 NUMERICAL METHODS

2.1 N-body+SPH simulations

The numerical methods and simulations used in this study have, to a major part, been presented in previous papers (Karl et al. 2010, 2011). Here, we will briefly summarize the most important facts and describe the new simulations in more detail. The simulations were performed using the parallel Tree/SPH code Gadget3 (see Springel 2005) including cooling, star formation and thermal stellar feedback as detailed below.

Following Katz et al. (1996), radiative cooling is computed for an optically thin plasma out of primordial hydrogen and helium, assuming ionization equilibrium in the presence of a spatially uniform and time-independent local UV background (Haardt & Madau 1996). Star formation and feedback are treated using the effective multi-phase model by Springel & Hernquist (2003), where stars are allowed to form on a characteristic timescale $t_\star$ in regions where gas densities exceed a threshold $n_{\rm crit} = 0.129\,{\rm cm}^{-3}$. In these regions, the star-forming interstellar medium (ISM) is assumed to develop an effective two-phase fluid, where cold clouds are embedded in a hot ambient medium in pressure equilibrium. This is done by instantaneously returning mass and energy from massive short-lived stars to the ISM, where we choose a fraction of $\beta = 0.1$ in massive stars ($M_\star > M_\odot$) and $10^{51}\,{\rm erg\,s}^{-1}$ of energy released per supernovae.

As a result of the two-phase formulation, the "effective" equation of state (EOS) in star-forming regions is quite "stiff", providing a high and steeply rising pressure support to the gas with increasing density. A convenient way to parametrize uncertainties in the complex sub-grid physics is to control the efficiency of the thermal feedback via a further dimensionless parameter, $q_{\rm EOS}$ (see, e.g. Springel et al. 2005), which linearly interpolates between the full "stiff" feedback model ($q_{\rm EOS} = 1$) and a softer isothermal equation of state with $T = 10^4$ K ($q_{\rm EOS} = 0$). Recently, Hopkins &

⋆ E-mail: skarl@ast.cam.ac.uk

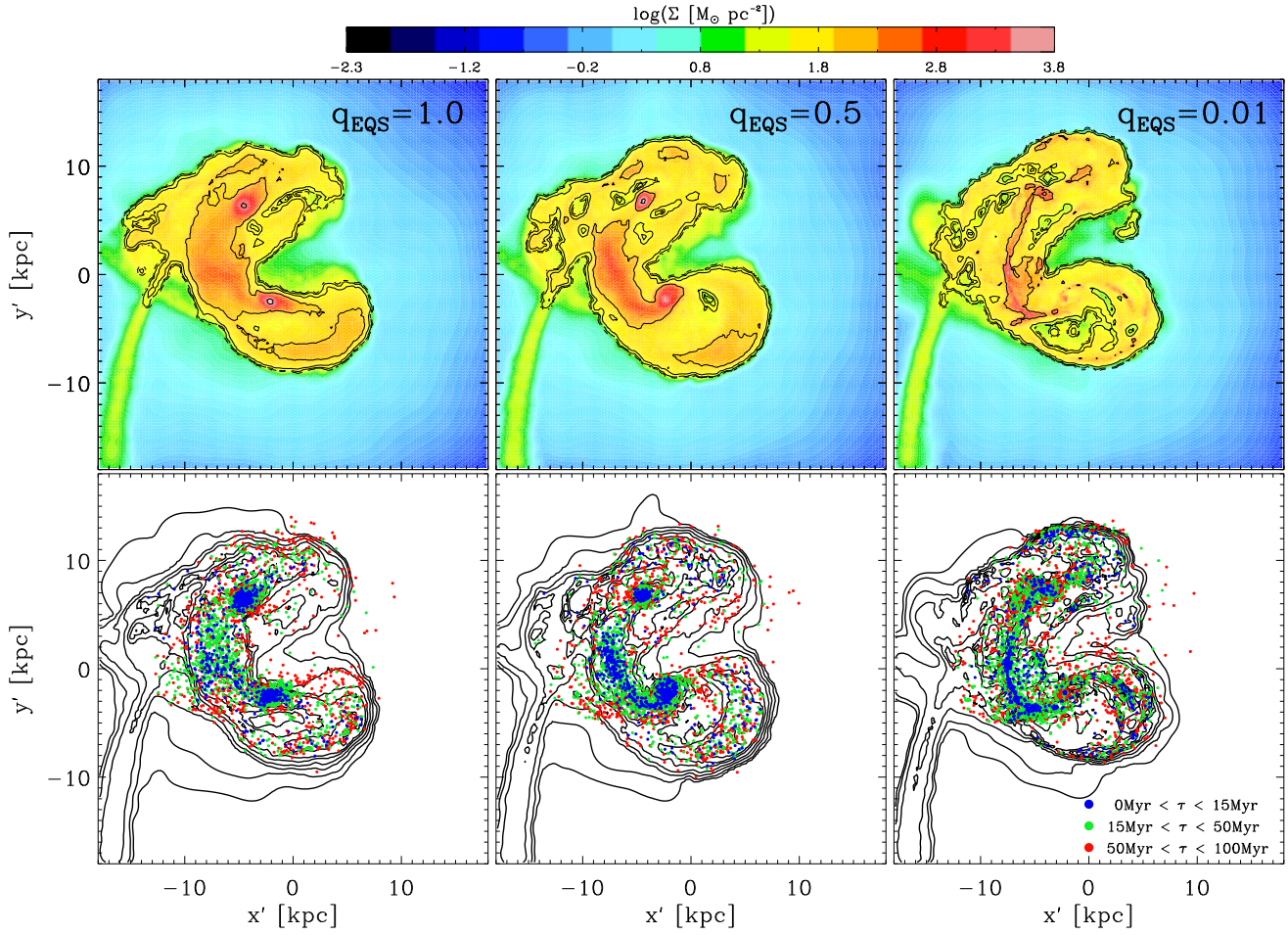

Figure 1. Projected gas surface density and star formation in the central ±18 kpc of the simulated disks for three values of the parameter for the softened equation of state, $q_{\rm EOS} = 1.0$ (*left*), $q_{\rm EOS} = 0.5$ (*middle*), and $q_{\rm EOS} = 0.01$ (*right*). *Upper panels:* Projected gas surface density overlain with contours of the the star formation rate surface density. The contours correspond to levels of $\log(\Sigma_{\rm SFR} / M_\odot\,{\rm yr\,kpc^{-2}}) = -6, -5, \ldots, -3, -2$, respectively. *Lower panels:* Gas surface density contours and stellar particles formed within the last 100 Myr, color-coded by their age (see legend).

Quataert (2010) advocated a range of $q_{\rm EOS} = [0.125, 0.3]$ by comparing model predictions and simulations for different values of $q_{\rm EOS}$ to the gas properties in observed star forming systems. In this study, we test our Antennae models with various choices for $q_{\rm EOS}$ against changes in the quality of the match to Herschel-PACS observations in the far infra-red.

Motivated by comparable total magnitudes in the B- and R-band for both NGC 4038 and NGC 4039 (Lauberts & Valentijn 1989; de Vaucouleurs et al. 1991), we model the Antennae system as a 1:1 merger with a total mass of $M_{\rm tot} = 5.5 \times 10^{11}\,M_\odot$ for each galaxy. The initial disk models are set up following the method described in Springel et al. (2005). They all consist of a Hernquist (1990) cold dark matter halo with concentration parameter $c = 15$, exponential stellar and gaseous disks and a non-rotating Hernquist bulge with masses $[M_{\rm halo} = 5.0 \times 10^{11}\,M_\odot, M_{\rm disk,tot} = 4.1 \times 10^{10}\,M_\odot, M_{\rm bulge} = 1.4 \times 10^{10}\,M_\odot]$, respectively. In the model presented in Karl et al. (2010) and Karl et al. (2011) the disk is assumed to initially contain a fraction $f_{\rm g} = 20\%$ in gas ($M_{\rm disk} = 3.3 \times 10^{10}\,M_\odot$, $M_{\rm gas} = 8.3 \times 10^{9}\,M_\odot$). Here, we also study a new model which employs an initial disk gas fraction $f_{\rm g}^{4038} = 40\%$ in NGC 4038's disk, resulting in $M_{\rm disk} = 2.5 \times 10^{10}\,M_\odot$ and $M_{\rm gas} = 1.7 \times 10^{10}\,M_\odot$. For both models, we carried out a total of five runs each, varying the efficiencies of stellar feedback by using a softened equation of state parameter within $q_{\rm EOS} = (0, 0.01, 0.1, 0.5, 1)$. as detailed in Table 1. Otherwise, we use identical parameters for the progenitors except for the halo spin parameter λ, which directly influences the disk scale length of the galaxies (Mo et al. 1998) and, hence, the length of the tidal tails (Springel & White 1999). Our choice of $\lambda_{4038} = 0.10$ and $\lambda_{4039} = 0.07$ results in disk scale lengths of $r_{\rm d,\,4038} = 6.28$ kpc and $r_{\rm d,\,4039} = 4.12$ kpc (see Karl et al. 2010, for more details).

At our standard resolution, each galaxy consists of a total of $N_{\rm tot} = 1.2 \times 10^6$ particles with 4×10^5 dark matter particles, 2×10^5 bulge particles, and a total of 6×10^5 (stellar and gaseous) disk particles. The particle numbers are chosen such that we obtain a mass resolution of $m_{\rm bary} = 6.9 \times 10^4\,M_\odot$ with a gravitational softening length $\epsilon_{\rm bary} = 35$ pc in all baryonic components, while dark matter halo particles have a mass of $1.2 \times 10^6\,M_\odot$ with $\epsilon_{\rm DM} = 150$ pc.

Table 1. Characteristics and nomenclature for the numerical models.

Model[1]	$q_{\rm EOS}$	$f_{\rm g}^{4038}$
K10-Q0	0	20%
K10-Q0.01	0.01	20%
K10-Q0.1	0.1	20%
K10-Q0.5	0.5	20%
K10-Q1	1	20%
F40-Q0	0	40%
F40-Q0.01	0.01	40%
F40-Q0.1	0.1	40%
F40-Q0.5	0.5	40%
F40-Q1	1	40%

In the standard K10 models, this yields 4.8×10^5 stellar and 1.2×10^5 gas particles in the galactic disks, while, in the K10F40 models, where we double the disk gas fraction in NGC 4038, we accordingly employ 3.6×10^5 stellar and 2.4×10^5 gas particles.

The initial interaction orbit is set identical to the one presented in Karl et al. (2010), i.e. a mildly elliptic prograde orbit with initial separation $r_{\rm sep} = r_{\rm vir} = 168\,{\rm kpc}$ and pericentric distance $r_{\rm p} = r_{\rm d,\,4038} + r_{\rm d,\,4039} = 10.4\,{\rm kpc}$, where $r_{\rm vir}$ and $r_{\rm d}$ are the virial radius and disk scale length, respectively. With disk inclinations $i_{4038} = i_{4039} = 60^\circ$ and pericentric arguments $\omega_{4038} = 30^\circ$ and $\omega_{4039} = 60^\circ$ this orbit has proven to result in a very good agreement with the observed large- and small-scale morphology and line-of-sight kinematics of the Antennae at the time of best match.

2.2 Radiative transfer calculations

In Section 3, we compare synthetic far infra-red (FIR) maps from our Antennae models with recent data by Klaas et al. (2010), obtained with the Herschel-PACS instrument. We describe here the post-processing procedure applied to our simulations to construct the synthetic FIR maps.

The FIR emission in star-forming galaxies is generally dominated by thermal emission from dust that has been heated by stellar radiation **(citations , e.g. KINGFISH)**. Due to strong spatial fluctuations in both dust density and stellar emission, the dust temperature varies in a very complicated manner. To produce accurate FIR maps of the galaxy it is therefore necessary to run 3D radiative transfer (RT) simulations of the SPH galaxy model.

Maps are produced by post-processing SPH snapshots with our dust RT code (Lunttila et al., in preparation). This code is based on the Monte-Carlo RT code by Juvela (2005), though much of it has been thoroughly updated or re-written from scratch. Before starting the RT calculations, the SPH snapshot is gridded adaptively onto an adaptive mesh refinement (AMR) grid using the SPH smoothing kernel. The use of an adaptive grid enables good spatial resolution in the dense inner parts of the galaxy while keeping the total number of computational cells in the grid low. In the simulations described in this paper the size of the parent grid is 80 kpc while the minimum cell size is 78.125 pc, resulting in an effective resolution of 1024^3. The total number of cells in the mesh refinement grid is typically $\sim 2 \times 10^6$.

Interstellar dust is assumed to be uniformly mixed with the gas, and a single dust model is used in the whole galaxy. The dust is assumed to have average properties as found in the Milky Way (Draine 2003)[2], with gas-to-dust ratio of 124 and $R_{\rm V} \equiv \frac{A_{\rm V}}{E(B-V)} = 3.1$, where $A_{\rm V}$ is the V-band extinction and $E(B-V)$ defines the "color excess". Stellar emission is modeled by assigning (Bruzual & Charlot 2003) spectral energy distributions (SEDs) to all star particles according to their ages. Because our N-body+SPH simulations do not track metallicity, we assume $Z = 0.02$ ("solar abundance" Anders & Grevesse 1989) for all stellar particles, i.e. disk, bulge, and newly formed stellar particles, which is in reasonable agreement with estimates from young star clusters in the Antennae (e.g. Bastian et al. 2009; Brandl et al. 2009). Stellar particles existing at the start of the SPH simulation are assigned ages uniformly distributed between 0 and 4 Gyr for the disk stars **(Peter: maybe, exponential SFH with mean of 4 (?) would be better!)** and between 3 and 7 Gyr for the bulge. Stellar particles formed over the course of the simulation have their ages assigned simply corresponding to the time elapsed since their formation. Note that a slightly different choice for the particular disk and bulge ages will not change the FIR emission dramatically since it is dominated by the heating of the dust by young stars, i.e. the stars formed in the simulations depending on the different star formation histories. After the dust distribution and radiation sources are set up, the RT simulation is used to calculate the dust equilibrium temperatures. The calculation is run iteratively to account for the dust self-absorption and heating, until the dust temperatures have converged.

As a final step in the RT simulations, 70 μm, 100 μm, and 160 μm maps are produced using the previously computed dust temperatures. The maps are then convolved to the resolution of the Herschel-PACS instrument at the corresponding wavelengths to simulate the observations by (Klaas et al. 2010). The full-width-half-maximum (FWHM) of the point-spread function (PSF) is $5''.5$, $6''.8$, and $11''.8$ in the $70\,\mu m$, $100\,\mu m$, and, $160\,\mu m$ bands, respectively. Further details on the RT model parameters are summarized in Table 3.

(**Better results could be obtained by 1) using the exact Herschel PSF; 2) visually, by using the colour table as Klass. 2010. Both issues have already been discussed with U. Klaas.**)

3 SIMULATED STAR FORMATION PROPERTIES IN THE ANTENNAE MODELS

Check: Herrera,C. and Ueda, J. 2011/12

In the upper panels of Figure 1 we show color-coded

[2] http://www.astro.princeton.edu/?/draine/dust/dustmix.html

maps of the total gas surface densities, $\Sigma_{\rm gas}$, obtained in the central ± 18 kpc of three simulations with a different choice in the adopted equation of state for the multi-phase ISM ($q_{\rm EOS} = 1.0$, $q_{\rm EOS} = 0.5$, and $q_{\rm EOS} = 0.01$, from left to right). Each gas surface density map is overlaid with contours of the SFR surface density $\Sigma_{\rm SFR}$. For all three parameters, the overall morphology is similar: The nuclei of the progenitor disks are still well distinct, but connected by a ridge of high density gas. In the case of strong feedback, a high-density overlap region has formed, but the highest densities are found in the galactic centers. In the simulations with less vigorous feedback, however, the high surface density regions tend to become more pronounced in the overlap (middle and right upper panels). As a consequence we also find an increasing number of low-density ("void") regions inside the disks for lower values of $q_{\rm EOS}$ due to the decreasing pressure support in the star-forming gas. The star formation contours directly support this picture. Lowering the effective pressure, and hence the stellar feedback, in star forming regions leads to more confined, localized regions of intense star formation activity. Note that spatially confined areas of similar extent are observed in the overlap region in the Antennae (e.g. Mirabel et al. 1998; Zhang et al. 2001; Wilson et al. 2000; Wang et al. 2004; Zhang et al. 2010). In the lower panels of Figure 1, we show the corresponding contours in the gas surface density and overplot color-coded all stellar particles (with individual masses of $m_{\rm star} = 6.9 \times 10^4 M_\odot$) formed in the last $\tau < 15$ Myr (blue), $15\,{\rm Myr} < \tau < 50\,{\rm Myr}$ (green), and $50\,{\rm Myr} < \tau < 100\,{\rm Myr}$ (red). This period corresponds to the time span of the interaction-induced rise in the star formation activity during the recent second encounter. The youngest stars (blue) form predominantly in regions of currently high gas densities, i.e. in the centers, the overlap region, and in the arc-like features along the disks, very similar to observations of the youngest clusters in the Antennae (Whitmore et al. 1999, 2010; Wang et al. 2004, see also Section 1**(intro!)**). This quantitatively confirms our earlier results with a particular choice of $q_{\rm EOS} = 0.5$ (Karl et al. 2010), indicating that our conclusions are robust to altering the specifics of our adopted star formation algorithm. However, a more detailed analysis of Figure 1 also shows that the star formation in the galaxy centers is much more pronounced in the run with $q_{\rm EOS} = 1.0$ (lower left panel), while the overlap starburst gains more and more in relative importance for $q_{\rm EOS} = 0.5$ and $q_{\rm EOS} = 0.01$ (see below). Furthermore, young stars ($\tau < 50$ Myr) tend to have formed more commonly both in the overlap region and well-defined arcs in the remnant spirals, while older stars ($50\,{\rm Myr} < 100\,{\rm Myr}$) are dispersed more evenly throughout the disks. This exactly captures a similar trend observed in the Antennae (e.g. Zhang et al. 2001, Figure 2). Therefore we confirm that, within a range of sensitive choices of $q_{\rm EOS}$, the overlap starburst seems to driven by the most recent episode of star formation in the Antennae, which was induced by the second close encounter.

Using high-resolution mid-IR Spitzer spectroscopy within a $5 - 38\,\mu m$ wavelength range, Brandl et al. (2009) was able to derive spatially resolved SFRs in a number of selected regions in the Antennae. By converting their measured mid-IR luminosities to SFRs using a Kennicutt-Schmidt relation (Kennicutt 1998), they obtain upper limits for the SFRs of $0.63\,M_\odot\,{\rm yr}^{-1}$ and $0.33\,M_\odot\,{\rm yr}^{-1}$ in the nuclei of NGC 4038 and NGC 4039, and $5.4\,M_\odot\,{\rm yr}^{-1}$ when co-adding the five infrared peaks in the overlap region. More recently, thanks to the very good spatial resolution of the Herschel-PACS instrument in the FIR regime, Klaas et al. (2010) could augment the previously determined IR SEDs of individual star-forming knots by additional flux estimates in $70\,\mu m$, $100\,\mu m$, and $160\,\mu m$ in the central disks and the two nuclei. This allows for very precise determination of the total FIR luminosity in individual knots resulting in integrated values of $L_{\rm FIR}^{4038} = 1.17\,M_\odot\,{\rm yr}^{-1}$ and $L_{\rm FIR}^{4039} = 0.50\,M_\odot\,{\rm yr}^{-1}$ in the nuclei of NGC 4038 and NGC 4039, and a total of $L_{\rm FIR}^{\rm OvL} = 4.84\,M_\odot\,{\rm yr}^{-1}$ summing over all knots in the overlap region (see their Table 2). We compare these values to our simulated SFRs in the galactic nuclei of NGC 4038 and NGC 4039 (defined as the central region of each nucleus with a radius of 1 kpc), and the overlap region (chosen according to the central morphology of the simulations). Details are provided in Table 2, where we compare for each simulation the different specific regions (see 2nd and 3rd column) to a number of quantities of interest given in columns (4) – (6). We find a trend that, while in the case of strong feedback ($q_{\rm EOS} = 1.0$, $q_{\rm EOS} = 0.5$), the simulations fall short of producing the most intense starburst in the overlap compared to only a modest star formation activity in the two nuclei, in the simulation with $q_{\rm EOS} = 0.01$, a very vigorous overlap starburst with a SFR of $\sim 11\,M_\odot\,{\rm yr}^{-1}$ develops. This run actually yields a SFR in this region that is even higher than the observed estimate (by a factor of ~ 2), with a very low ratio of ${\rm SFR_{overlap}/SFR_{nuclei}} = 0.09$ compared to ~ 0.35 in the Herschel-PACS observations. The total instantaneous SFR of $14.32\,M_\odot\,{\rm yr}^{-1}$, as measured from the simulated SPH particles, is also in very good agreement with the range of observed values between $\sim 5 - 20\,M_\odot\,{\rm yr}^{-1}$ (e.g. Zhang et al. 2001), and in good approximate agreement (factor of ~ 1.5) with the value of $22.2\,M_\odot\,{\rm yr}^{-1}$ advocated by Klaas et al. (2010). In addition, the latter value compares favorably with respect to the other two simulations with SFR $= 7.16\,M_\odot\,{\rm yr}^{-1}$ for $q_{\rm EOS} = 1.0$ and SFR $= 8.74\,M_\odot\,{\rm yr}^{-1}$ for $q_{\rm EOS} = 0.5$, respectively. Therefore, without attempting a fine-tuned match, we conclude that adopting a rather low feedback efficiency for the stellar feedback seems to give the most consistent results with the observational estimates.

What is the reason for such different SFRs in the galactic nuclei and the overlap in the simulations with three different $q_{\rm EOS}$? A glimpse at Figure 2 reveals a possible explanation. All three simulations show a steady decrease in their gas mass (upper solid line) from the very start of the simulations, corresponding to a gradual build-up of the new stellar component (blue solid line). However, due to the lower pressure support in the effective multi-phase model in the case of the low-feedback simulation (lower panel), a fraction of $\sim 12\%$ of the initial gas mass have already been turned into stars by the time of the first pericenter (blue dots), whereas the two simulations with stronger feedback (upper and middle panels) have only consumed about $\sim 6\%$ ($q_{\rm EOS} = 1.0$) and $\sim 8\%$ ($q_{\rm EOS} = 0.5$) at the same time. The total amount of non-star-forming gas (blue) stays constant to within $\sim 10\%$ during the whole course of the

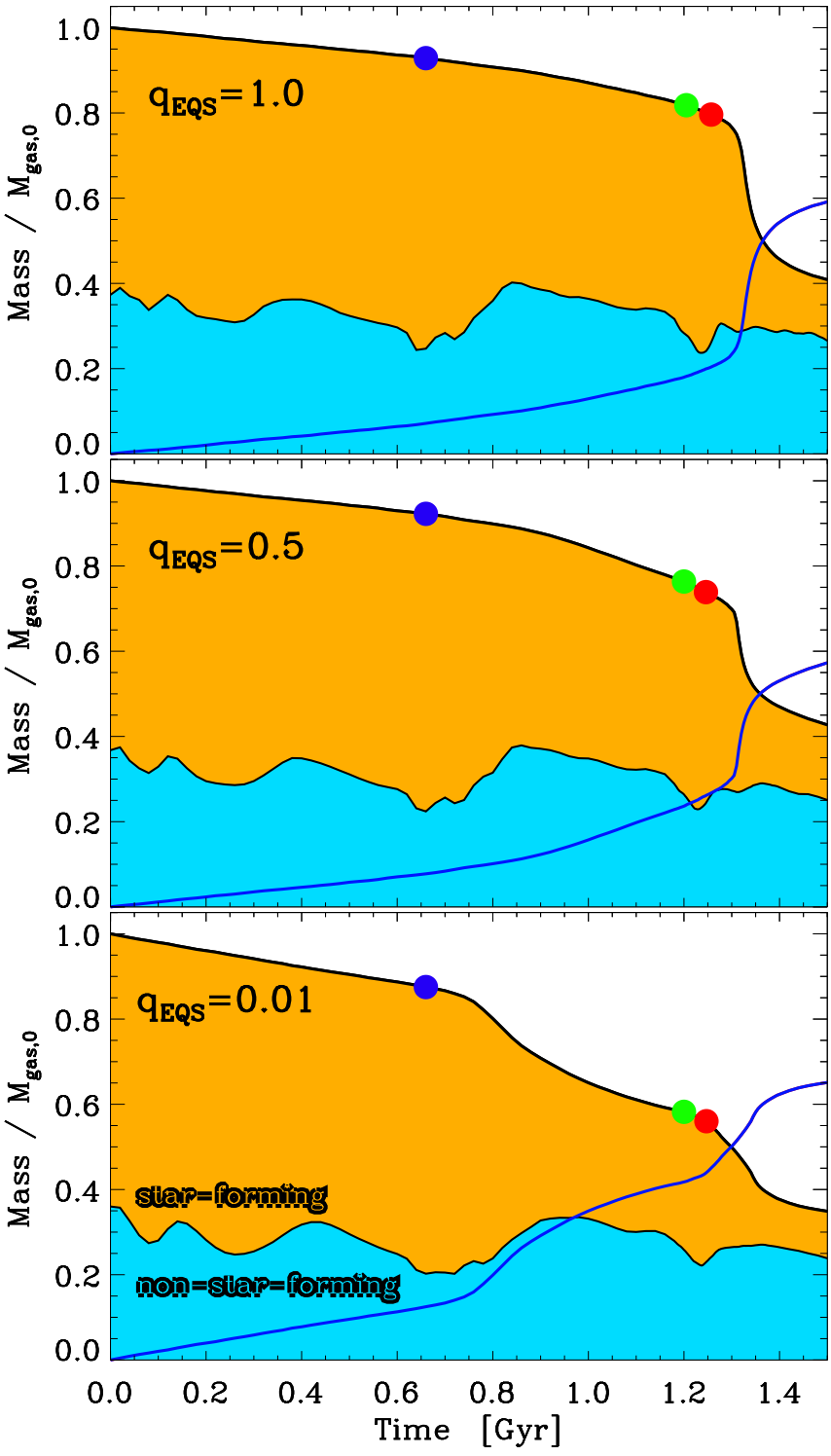

Figure 2. Time evolution of the mass in gas (upper black solid line) and newly formed stars (blue line) normalized to the initial gas mass in three simulations with different parameters for the softened equation of state. *Upper panel:* full feedback model $q_{\rm EOS} = 1.0$; *middle panel:* intermediate feedback model, $q_{\rm EOS} = 0.5$; and *lower panel:* model with very weak feedback $q_{\rm EOS} = 0.01$. In addition, we distinguish between the dense star-forming gas ($n > n_{\rm crit} \equiv 0.128\,{\rm cm}^{-3}$) treated by the effective multi-phase model (yellow) and non-star-forming gas (blue). The blue, green and red dots indicate the times of first pericenter, second pericenter, and the time of best match in each simulation.

Table 2. Relative star formation rates between the nuclei and the overlap region in three different simulations with $q_{\rm EOS} = 1.0$, $q_{\rm EOS} = 0.5$, and $q_{\rm EOS} = 0.01$.

Simulation	Region	Area	$N_\star/N_\star^{{\rm tot}\,a}$	$N_\star(<1\,{\rm Myr})^b$	SFR $[M_\odot\,{\rm yr}^{-1}]$
$q_{\rm EOS} = 1.0$	$\rm Nuc_{4038}$	$r = 1\,{\rm kpc}$ at $(-4.4, 6.3)\,{\rm kpc}$	10.6 %	25	1.71
	$\rm Nuc_{4039}$	$r = 1\,{\rm kpc}$ at $(-1.7, -2.7)\,{\rm kpc}$	32.1 %	53	4.08
	Overlap	$x \in [-10, -3.8]\,{\rm kpc}$, $y \in [-3, 5]\,{\rm kpc}$	9.6%	10	0.49
$q_{\rm EOS} = 0.5$	$\rm Nuc_{4038}$	$r = 1\,{\rm kpc}$ at $(-4.25, 6.9)\,{\rm kpc}$	15.4%	62	4.55
	$\rm Nuc_{4039}$	$r = 1\,{\rm kpc}$ at $(-2.3, -2.1)\,{\rm kpc}$	38.1%	40	2.85
	Overlap	$x \in [-9.5, -3.8]\,{\rm kpc}$, $y \in [-5., 6.]\,{\rm kpc}$	10.6%	27	0.76
$q_{\rm EOS} = 0.01$	$\rm Nuc_{4038}$	$r = 1\,{\rm kpc}$ at $(-4.4, 7.5)\,{\rm kpc}$	10.5%	8	0.49
	$\rm Nuc_{4039}$	$r = 1\,{\rm kpc}$ at $(-2.1, -3.1)\,{\rm kpc}$	28.5%	5	0.44
	Overlap	$x \in [-10.5, -3.2]\,{\rm kpc}$, $y \in [-5.5, 6.]\,{\rm kpc}$	15.4%	177	10.88

[a] number of new stars in the analyzed area compared to the total number of new stars
[b] the number of new stars with ages $\tau < 1\,{\rm Myr}$

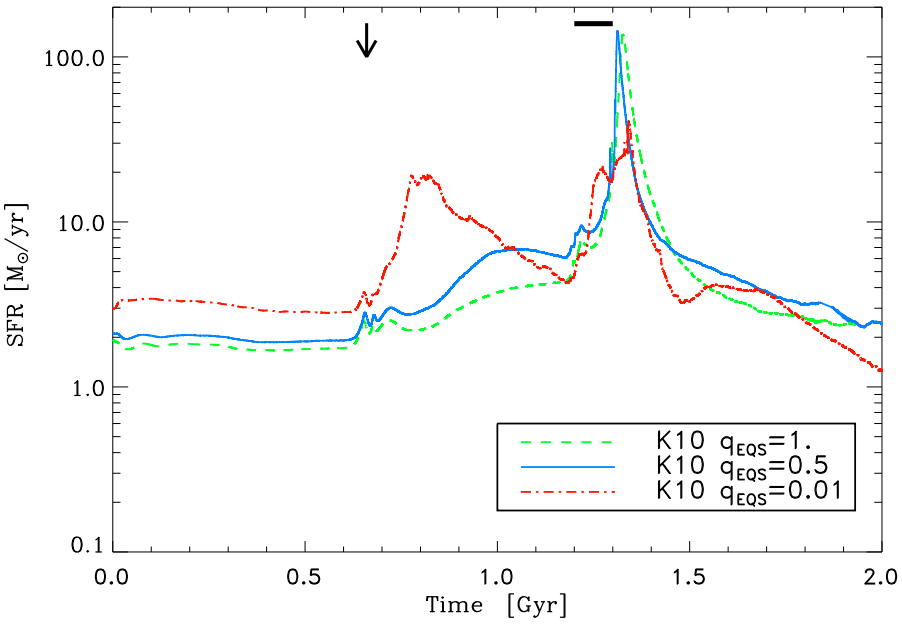

Figure 3. Star formation histories for three Antennae simulations with different parameters for the softened equation of state: full (green, $q_{\rm EOS} = 1.0$), intermediate (blue, $q_{\rm EOS} = 0.5$) and weak feedback (red, $q_{\rm EOS} = 0.01$). The arrow gives the time of first close encounter, while the bar indicates the time between second close encounter and final merger.

simulated time span ($t < 1.5\,{\rm Gyr}$), save some little 'dips' associated with the first and the second pericenter passages ($t = 0.66\,{\rm Gyr}$ and $t = 1.20\,{\rm Gyr}$). The more dramatic evolution can be seen in the star-forming gas (yellow) which gets efficiently depleted after the first pericenter in the simulation with weak feedback (lower panel), having consumed more than $\sim 40\%$ of the initial gas at the time of second pericenter (green dots). In contrast, in the full-feedback run there are still about 80% of the initial gas mass remaining after the second encounter (green dots), which leads to a very rapid consumption of $\sim 40\%$ of the gas within the first $\sim 100\,{\rm Myr}$ after the final merger (red dots). This is

the reason why in the model with weak stellar feedback a large fraction of the high-density gas in the galactic nuclei has already formed stars during the first encounter such that, after the second encounter, the star formation in localized density peaks of shocked gas in the overlap region gains drastically in relative importance with respect to the nuclear star formation. **(Peter: hand-waving! Why so much gas left in overlap and not in nuclei?)**

A complementary view of this picture is offered by the star formation histories in the three simulations (Figure 3), where, to guide the eye, we indicate the time of first pericentre and the time between second encounter and final merger by a thick downward arrow and the horizontal bar, respectively. While the simulations with $q_{\rm EOS} = 1.0$ (green dotted line) and $q_{\rm EOS} = 0.5$ (blue solid line) show very similar SFRs initially, the SFR for the $q_{\rm EOS} = 0.01$ simulation is larger by a factor of ~ 2 from the very start. After the first pericenter (black arrow), the low-feedback run experiences a significant rise in the SFR by almost a factor of ten, while the other two simulations show a more gradual increase. However, while the low-feedback simulation shows a higher total SFR of $\sim 14\,M_\odot\,{\rm yr}^{-1}$ at the time of best match, powered by the short-lived overlap starburst shortly after the second pericenter, the other two simulations build up very powerful nuclear starbursts after the final merger with maximum total SFRs of ${\rm SFR}_{\rm max} \sim 140\,M_\odot\,{\rm yr}^{-1}$. An equally powerful starburst does not develop in the case of weak feedback (with ${\rm SFR}_{\rm max} = 40.8\,M_\odot\,{\rm yr}^{-1}$). The reason for the latter can be accounted to two different facts. First, due to a more rapid gas consumption during the first pericentre, dense star-forming gas is depleted by a larger fraction in the two nuclei than in the stronger feedback case. And, second, weaker pressure support in the star-forming gas phase in the $q_{\rm EOS} = 0.01$ case makes the gas in the overlap region more susceptible to local shock-induced fragmentation and subsequent star formation. **(Simon: this needs to be checked in detail, again.)**

4 COMPARISONS WITH OBSERVATIONS

In the Antennae galaxies, the most intense star bursts take place in regions that are heavily obscured in the optical (Mirabel et al. 1998), but can be seen at longer wavelengths due to heated dust grains that re-process the UV radiation of young stars (Vigroux et al. 1996; Wang et al. 2004; Klaas et al. 2010). However, the simulations presented in this and our previous papers do not include models for the formation of molecular gas and dust. Therefore, we use an adaptive 3D radiative transfer algorithm to post-process our simulation outputs, as detailed in Section 2.2, to assess the FIR dust emission expected from our simulated data.

In Figure 4 we compare FIR maps at 70 μm, 100 μm, and 160 μm with observations by Klaas et al. (2010). Emission from these bands, in general, reveals the sites of hidden recent star formation, that are still embedded in the dusty molecular clouds from which they have formed. We obtain very reassuring agreement between simulations and observations. In particular, the simulated 70 μm, 100 μm, and 160 μm maps all trace the same characteristic sequential locations of the well-confined star-forming regions in the overlap in a very similar way to Figure 1 in Klaas et al. (2010), which we have reproduced in the lower row of Figure 4 for better comparison. In addition, the simulated maps recover the locations of individual star-forming knots in the overlap area very well in all three bands compared to similar knots in the Antennae. However, the simulations show additional knotty sub-structure in the northern overlap region which is not detected at a similar level in the observations. We find that the brightest emission in all three bands comes from the overlap region. More specifically, more than 50% of the simulated FIR emission in the three bands originates from the overlap region, compared to only $\lesssim 10\%$ from the two nuclei in NGC 4038 and NGC 4039 combined. A similar percentage (6-8 %) is detected from the two nuclei in the observations in all three Herschel-PACS bands. The combined emission from knots K1 to K4 gives a lower bound for the total emission from the overlap region, yielding a total of $\sim 15-25\%$ for the three different bands. However, detailed inspection reveals similar differences in the spatial distribution of the simulated and observed FIR emission as in the HI observations. All three upper panels in Figure 4 show substantial emission from the southern disk (NGC 4039) that is not seen in the observations (lower panels). This makes the observed disks also look slightly more "tilted" than the simulated ones. Note, however, that this discrepancy is remedied to some extent in the Herschel 160 μm map, which has twice the exposure time than the observations in the 70 μm and 100 μm bands. Similarly, we do not find equally strong emission for the progenitor disks, including the arc-like feature in the northern spiral, as is detected in the 100 μm and 160 μm Herschel maps (note also the adopted lower limits in the simulated FIR maps). This may partly be caused by the weak stellar feedback adopted in the simulation, leading to very high local gas densities in the overlap region relative to the rest of the disks, which, in turn, is seen in our simulated FIR maps.

Table 3. Model parameters of the radiative transfer calculations.

Property	RT parameter
constant gas-to-dust ratio	124 : 1
extinction law	$R_{\rm V} = 3.1$
dust model	Draine (2003)
stellar emission model	Bruzual & Charlot (2003)
metallicity	$Z = 0.02$
ages for disk particles	0 - 4 Gyr
ages for bulge particles	3 - 7 Gyr

As a consistency test, we also constructed a simple CO-map from our simulations in order to compare to another widely used star formation tracer. Hereby, we first invoke the amount of molecular H_2 from the SFR of the simulated gas particles by using an "inverse" Bigiel et al. (2008) relation of the form

$$\Sigma_{\rm H_2} \;=\; 10 \cdot \left(\frac{\Sigma_{\rm SFR}}{A}\right)^{1/N} M_\odot\,{\rm pc}^{-2}. \qquad (1)$$

where, $\Sigma_{\rm H_2}$ and $\Sigma_{\rm SFR}$ are the surface densities in H_2 and the

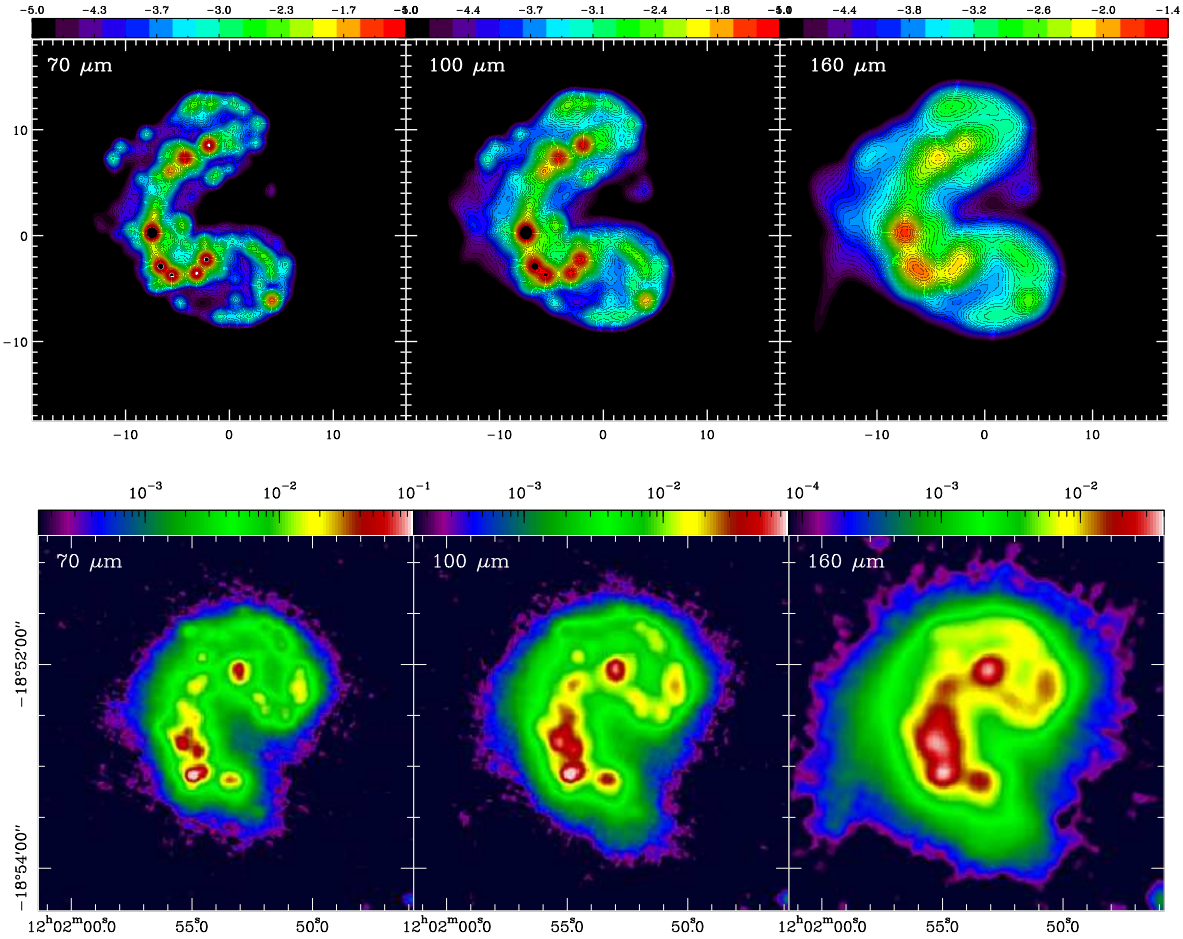

Figure 4. Synthetic observations of the inner region of the Antennae at 70 μm *(left column)*, 100 μm *(middle column)*, and 160 μm *(right column)* from the fiducial simulation with $q_{\rm EOS} = 0.01$ *(upper panels)*, obtained by using 3D radiative transfer calculations. These are compared to Herschel-PACS observations in the same bands from Klaas et al. (2010, ; *lower panels*). **(Colour-table, PSF, units, log-scale!)**

SFR, respectively, and the latter is given in $M_\odot\,{\rm yr}^{-1}\,{\rm kpc}^{-2}$. **(Peter: Motivation for this?)** A is a normalization constant with $\log(A) = -2.06$, and $N = 0.96$ is a power-law index near unity (see Bigiel et al. 2008, Equation 2 and Table 2). Then, we relate the H_2 masses back to CO by adopting the same CO-to-H_2 conversion factor (see Wilson & Scoville 1990), i.e. $M_{\rm mol} = 1.61 \times 10^4\, d^2_{\rm Mpc}\, S_{\rm CO}\, M_\odot$, where $S_{\rm CO}$ is given in $Jy\ {\rm km\,s}^{-1}$ and we $d_{\rm Mpc} = 19$ as given in Wilson et al. (2000) for a fair comparison. We show the synthetic CO map in the left panel of Figure 6, compared to an integrated CO map (taken form Figure 1 in Wilson et al. 2000). Since we find it hard to exactly match the contours in the observations (right panel in Figure 6), we adopt a very similar, but slightly larger contour range. In particular, we use the same contour range as the observations, putting additional contours at 0.01 and 100, 120, 140, 160 Jy/beam ${\rm km\,s}^{-1}$ to account for the larger range in the simulations. In the synthetic CO map (left panel in Figure 6) we find the CO emission to be entirely confined to the central regions of the merger in a number of distinct high-density peaks in the southern overlap and near the two nuclei. To a lesser extent, we also find emission from two arcs along the southern and northern remnant spirals. The observations exhibit a strikingly similar picture (see right panel in Figure 6). The strongest emission peaks from the CO(1-0) transition are detected in the two galactic nuclei, the overlap region, and the north-western spiral arc in NGC 4038, whereas, again, there is no emission in the southern disk as detected at a very low level in the simulation. **(Peter: check also Narayanan papers on RT with CO-lines!)**

Comparing with Figure 4, we find that the peaks of both FIR and CO emission coincide very well in the southern part of the overlap region. This is also seen in multi-wavelength comparisons of the Antennae galaxies (e.g., Haas et al. 2000; Klaas et al. 2010), where, e.g. the highest peak at 100 μm, east of the southern nucleus (Klaas et al. 2010, knot "K1"), includes the super-giant molecular cloud complexes SGM3 - SGM5 (indicated in the right panel of Figure 6). Similarly, other luminous FIR emission peaks (knots "K2a" and "K2b") are identified with the CO complexes SGM 1 and SGM 2, as well as with peaks number 3 and 4 on radio maps by Hummel & van der Hulst (1986). Note that the latter two FIR knots together

encompass the brightest emission region at 160 μm and are located to the north of knot K1 in the highly obscured part of the overlap region (see Figure 3 in Klaas et al. 2010).

Finally, we compare the observed and the simulated SEDs in Figure **TBD! Needs to be written here**.

5 DISCUSSION AND CONCLUSIONS

In this work, we have Distances (for fg40 0-1 model -¿ factor of 2 in flux difference would correspond very well to distance of 22 Mpc to the Antennae), mgas, mdust (also scaled w/ distance).
Exp. SFH.
Gas Halo; AGN;
Phil Hopkins (q=0), range advocated, more physics (feedback).
Findings: 0) no(t much) difference when including noise; i) much more diff. between numerical models than between post-processing assumption (what did we vary there? dust, check exp SFH!).
ii) Distance shorter -¿ higher flux; more gas -¿ higher flux; more dust -¿ better colours in SED; lower Q better morphology; sweet-spot in fluxes / gas available / susceptibility for starburst.
Self-gravity for FG40 q=0; not for FG20 q=0;

ACKNOWLEDGMENTS

We thank ... and an anonymous referee for very useful comments that improved the presentation of the paper.

REFERENCES

Anders E., Grevesse N., 1989, Geochim. Cosmochim. Acta, 53, 197
Bastian N., Trancho G., Konstantopoulos I. S., Miller B. W., 2009, ApJ, 701, 607
Bigiel F., Leroy A., Walter F., Brinks E., de Blok W. J. G., Madore B., Thornley M. D., 2008, AJ, 136, 2846
Brandl B. R. et al., 2009, ApJ, 699, 1982
Bruzual G., Charlot S., 2003, MNRAS, 344, 1000
de Vaucouleurs G., de Vaucouleurs A., Corwin, Jr. H. G., Buta R. J., Paturel G., Fouque P., 1991, Third Reference Catalogue of Bright Galaxies, de Vaucouleurs, G., de Vaucouleurs, A., Corwin, H. G., Jr., Buta, R. J., Paturel, G., & Fouque, P., ed.
Draine B. T., 2003, ARA&A, 41, 241
Haardt F., Madau P., 1996, ApJ, 461, 20
Haas M., Klaas U., Coulson I., Thommes E., Xu C., 2000, A&A, 356, L83
Hernquist L., 1990, ApJ, 356, 359
Hopkins P. F., Quataert E., 2010, MNRAS, 407, 1529
Hummel E., van der Hulst J. M., 1986, A&A, 155, 151
Juvela M., 2005, A&A, 440, 531
Karl S. J., Fall S. M., Naab T., 2011, ApJ, 734, 11
Karl S. J., Naab T., Johansson P. H., Kotarba H., Boily C. M., Renaud F., Theis C., 2010, ApJ, 715, L88
Katz N., Weinberg D. H., Hernquist L., 1996, ApJS, 105, 19
Kennicutt, Jr. R. C., 1998, ARA&A, 36, 189
Klaas U., Nielbock M., Haas M., Krause O., Schreiber J., 2010, A&A, 518, L44+
Lauberts A., Valentijn E. A., 1989, The surface photometry catalogue of the ESO-Uppsala galaxies
Mirabel I. F. et al., 1998, A&A, 333, L1
Mo H. J., Mao S., White S. D. M., 1998, MNRAS, 295, 319
Springel V., 2005, MNRAS, 364, 1105
Springel V., Di Matteo T., Hernquist L., 2005, MNRAS, 361, 776
Springel V., Hernquist L., 2003, MNRAS, 339, 289
Springel V., White S. D. M., 1999, MNRAS, 307, 162
Vigroux L. et al., 1996, A&A, 315, L93
Wang Z. et al., 2004, ApJS, 154, 193
Whitmore B. C. et al., 2010, AJ, 140, 75
Whitmore B. C., Zhang Q., Leitherer C., Fall S. M., Schweizer F., Miller B. W., 1999, AJ, 118, 1551
Wilson C. D., Scoville N., 1990, ApJ, 363, 435
Wilson C. D., Scoville N., Madden S. C., Charmandaris V., 2000, ApJ, 542, 120
Zhang H., Gao Y., Kong X., 2010, MNRAS, 401, 1839
Zhang Q., Fall S. M., Whitmore B. C., 2001, ApJ, 561, 727

This paper has been typeset from a TEX/ LATEX file prepared by the author.

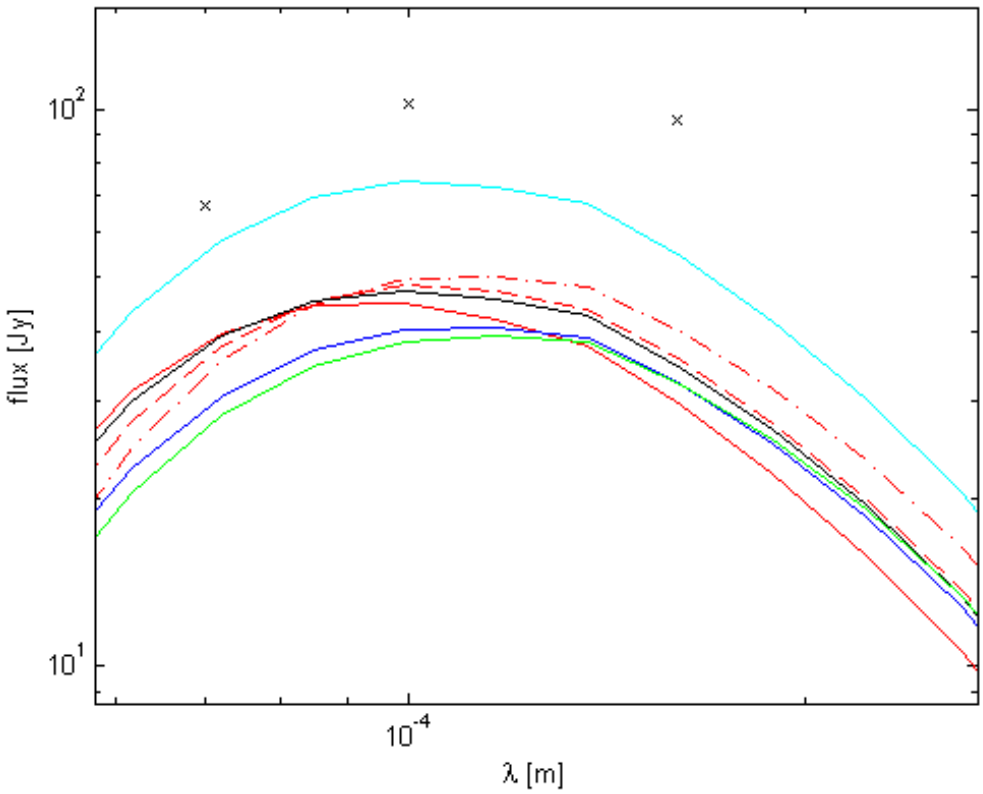

Figure 5. Comparison of total spectral energy distribution of the Antennae. Lines (Antennae simulations), Crosses (total Herschel fluxes at 70μm, 100mum and 160μm).

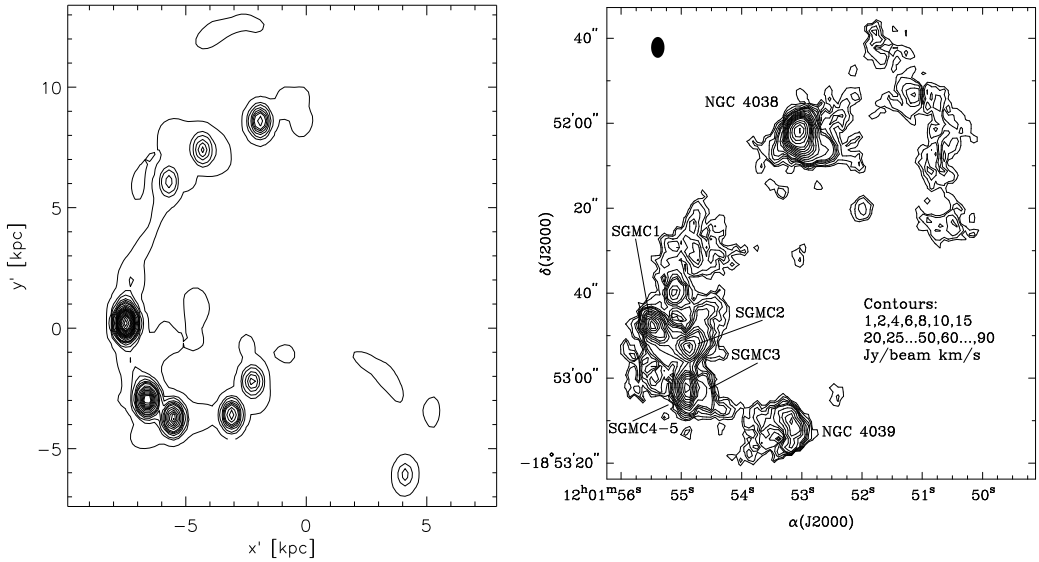

Figure 6. *Left panel:* Synthetic CO map of the inner regions of the Antennae from the fiducial simulation with $q_{\rm EOS} = 0.01$, where the integrated CO masses are obtained in a two-step process. H_2 surface densities are obtained from the SFR surface densities of the SPH particles using an "inverse" Bigiel et al. (2008) relation. Then, we apply the same CO-to-H_2 conversion factor as the observations to map the H_2 masses back to CO. *Right panel:* CO integrated intensity map, adapted from Figure 1 in Wilson et al. (2000). The two galactic nuclei and five super-giant molecular clouds in the overlap region are indicated. The filled black oval in the upper left corner gives the size of the synthesized beam in the observations.